Downloaded from orbit.dtu.dk on: Apr 26, 2024

DTU Library

Investigation of boron carbide and iridium thin films, an enabling technology for future x-ray telescopes

Massahi, S.; Christensen, F. E.; Ferreira, D. D. M.; Svendsen, S.; Henriksen, P. L.; Vu, L. M.; Gellert, N. C.; Jegers, A. S,; Shortt, B.; Bavdaz, M.

Total number of authors:
16

Published in:
Applied Optics

Link to article, DOI:
10.1364/AO.409453

Publication date:
2020

Document Version
Peer reviewed version

Link back to DTU Orbit

Citation (APA):
Massahi, S., Christensen, F. E., Ferreira, D. D. M., Svendsen, S., Henriksen, P. L., Vu, L. M., Gellert, N. C., Jegers, A. S., Shortt, B., Bavdaz, M., Ferreira, I., Collon, M., Landgraf, B., Girou, D. A., Sokolov, A., & Schoenberger, W. (2020). Investigation of boron carbide and iridium thin films, an enabling technology for future x-ray telescopes. *Applied Optics*, *59*(34), Article 10902. https://doi.org/10.1364/AO.409453

General rights
Copyright and moral rights for the publications made accessible in the public portal are retained by the authors and/or other copyright owners and it is a condition of accessing publications that users recognise and abide by the legal requirements associated with these rights.

- Users may download and print one copy of any publication from the public portal for the purpose of private study or research.
- You may not further distribute the material or use it for any profit-making activity or commercial gain
- You may freely distribute the URL identifying the publication in the public portal

If you believe that this document breaches copyright please contact us providing details, and we will remove access to the work immediately and investigate your claim.

To be published in Applied Optics:

Title: Investigation of boron carbide and iridium thin films, an enabling technology for future X-ray telescopes

Authors: Sonny Massahi,Finn Christensen,Desiree Della Ferreira,Sara Svendsen,Peter Henriksen,Lan Vu,Nis Gellert,Arne S Jegers,Brian Schortt,Marcos Bavdaz,Ivo Ferreira,Maximilien Collon,Boris Landgraf,David Girou,Andrey Sokolov,Waldemar Schoenberger

Accepted: 06 November 20

Posted 06 November 20

DOI: https://doi.org/10.1364/AO.409453

© 2020 Optical Society of America

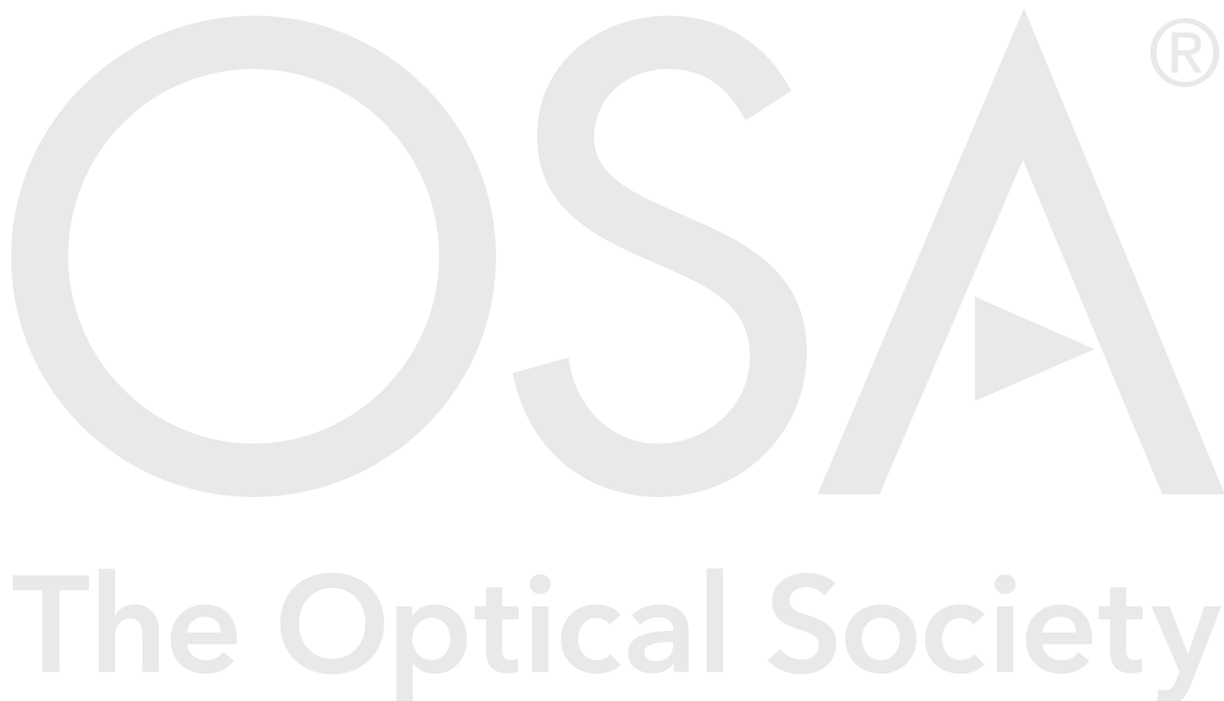

Investigation of boron carbide and iridium thin films, an enabling technology for future X-ray telescopes

S. Massahi[1,*], F.E. Christensen[1], D.D.M. Ferreira[1], S. Svendsen[1], P.L. Henriksen[1], L.M. Vu[1], N.C. Gellert[1], A. 'S Jegers[1], B. Shortt[2], M. Bavdaz[2], I. Ferreira[2], M. Collon[3], B. Landgraf[3], D. Girou[3,6], A. Sokolov[4], W. Schoenberger[5]

[1] *Technical University of Denmark, DTU, Elektrovej building 327, Kgs. Lyngby, Denmark*
[2] *European Space Research and Technology Centre, ESTEC, Keplerlaan 1, AZ Noordwijk, The Netherlands*
[3] *cosine measurement systems, Oosteinde 36, 2361 HE Warmond, The Netherlands*
[4] *Helmholtz-Zentrum Berlin fÃijr Materialien und Energie, BESSY-II, Albert-Einstein-Str. 15, 12489 Berlin, Germany*
[5] *Von Ardenne GmbH, Am Hahnweg 8, 01328 Dresden, Germany*
[6] *Huygens-Kamerlingh Onnes Laboratory, Leiden University, Postbus 9504, 2300 RA Leiden, The Netherlands*
[*] *sonmas@space.dtu.dk*

Abstract: We present an experimental examination of iridium and boron carbide thin film coatings for the purpose of fabricating X–ray optics. We use a combination of X–ray reflectometry and X–ray photoelectron spectroscopy to model the structure, composition, density, thickness and micro–roughness of the thin films. We demonstrate in our analyses how the two characterization techniques are complementary and from this we derive that an overlayer originating from atmospheric contamination with a thickness between 1.0–1.6 nm is present on the surface. The magnetron sputtered iridium films are measured to have a density of 22.4 g/cm^3. The boron carbide film exhibits a change in chemical composition in the top ~2 nm of the film surface when exposed to the ambient atmosphere. The chemical reaction occurring on the surface is due to an incorporation of oxygen and hydrogen present in the ambient atmosphere.
Lastly, we present a correlation between the absorption edges and the emission lines exhibited by the thin films in an energy range from 50–800 eV and the impact on the reflectivity performance due to contamination in thin films.

© 2020 Optical Society of America under the terms of the OSA Open Access Publishing Agreement

1. Introduction

Thin film coatings are an enabling technology for a vast number of applications. One application in particular is utilizing thin film technology in producing X–ray optics for space–borne X–ray telescopes [1]. A single layer or multilayer thin film coating of high quality, in terms of chemical stability, low micro–roughness, etc., is key for achieving the scientific objectives of any X–ray telescope mission.
The Advanced Telescope for High–ENergy Astrophysics (Athena) is a European Space Agency (ESA) selected mission [2], with the aim to describe the fundamentals of black hole growth and their influence on the Universe, and the assembly of ordinary matter into large scale structures [3, 4]. The photon energies wherein the scientific objectives for the Athena mission can be answered range from 0.1–12 keV.
The mission–enabling baseline thin film technology for Athena consists of iridium and a low–Z material. Iridium combined with a low–Z overlayer exhibits an excellent reflectance at grazing incidence in both the soft and hard X–ray regime [5, 6]. Boron carbide also referred to as

its chemical formula B_4C is a promising candidate as the low–Z material with its excellent reflectivity properties [7], however, its chemical composition and micro–structure is complex. As shown in [8, 9], thin films grown in "Zone 1" corresponding to the Thornton model [10] often exhibit voids due to the low adatom surface mobility, whereas thin films grown in "Zone T" in this model have compact structure. Moving from zone 1 to zone T requires a higher ratio between the substrate temperature and the melting temperature of the sputtered material. Understanding the true complexity of the boron carbide thin film structure is outside the scope of this work. However, mapping the impurities in the film is feasible using two characterization techniques; X–Ray Reflectometry (XRR) and X–ray Photoelectron Spectroscopy (XPS). These techniques are combined to model the thin film structure, density and composition.
The Athena optics are based on a state-of-the-art Silicon Pore Optics (SPO) technology involving multiple semiconductor industry processes utilized to produce innovative X-ray mirrors [11]. Process steps after the thin film deposition involve exposing the thin film samples to chemicals which can change the properties of the thin films [12]. Furthermore, exposure to the ambient atmosphere can alter the thin film composition [13] which would impact the performance of the optics. Performing ground-calibration is key to understand the long term behavior of the films which is critical for in orbit calibrations. This is a preliminary material study for the future calibration effort of the X–ray optics for the Athena mission.

2. Experimental Procedure

2.1. The thin film coating facility

The thin film coatings presented in this article were produced in the Athena dedicated coating facility [14]. The sputtering machine, BS1500S (Fig. 1), was commissioned as part of the effort to bring the Athena mirror plate coatings from an R&D level to an industrial scale. Initially, a market research was carried out with the aim of maximizing the mirror plate throughput and maintaining a high thin film quality. Numerous X–ray telescopes have adopted the Direct Current (DC) magnetron sputtering for deposition of reflective thin films with high film quality. Some of the other advantages by utilizing the magnetron sputtering technique are: low cost, high adhesion between thin films and substrate, good uniformity on large–area substrate, high reliability, excellent properties in terms of roughness and thickness uniformity and high deposition rates [15, 16].
The BS1500S is a drum coater similar to the DC magnetron unit operating at DTU Space, with which the majority of the NuSTAR mirrors were coated [17]. For the last decade, research and development of the thin film coatings for Athena has been performed at DTU Space [18–23]. The optical performance of the film coatings has been shown to meet the requirements for the Athena optics, though we are investigating long term stability and environmental resistance.

The BS1500S drum coater was fabricated by Von Ardenne GmbH and commissioned by DTU Space. The BS1500S can hold up to 14 substrate carriers on the carousel which has a diameter of 1.5 m. An Inverse Sputter Etcher (ISE) is integrated in the drum coater which is a key component to remove residual water and organics from the substrate surface prior to coating deposition, originating from the handling in ambient atmosphere. The ISE unit utilizes a mix of argon and oxygen ions to remove organic material on the substrate surface.
Two DC magnetrons are currently installed and a third magnetron will be installed allowing for tri–layer coatings. The magnetrons accommodate targets with a length of 600 mm long and a width of 108 mm which are bonded to a copper backing plate establishing a smooth electrical transition to the target as well as cooling of the target. The composition of the boron carbide target is 99.5% boron carbide, 0.2% iron, 0.2% silicon and 0.1% traces of other materials, and the iridium target has a purity of 99.9%.

OSA ® The Optical Society

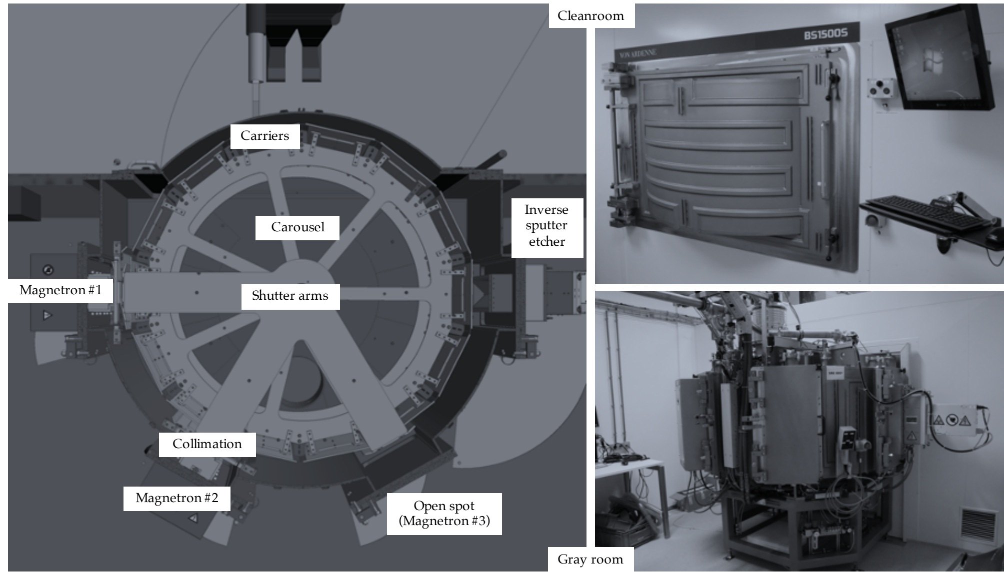

Fig. 1. Illustration and images of the BS1500S. The samples are mounted on a carousel inside the BS1500S. The sputtering direction is from outside towards inside.

The sputtered flux along the vertical direction of the magnetron varies which impacts the coating uniformity across the carrier. A honey comb collimator [24] was integrated in the chamber in the path between the target surface and the substrate surface to improve the quality of the film and the former mentioned uniformity. The target-to-substrate distance can be varied between 105.0 mm, 126.5 mm or 155.0 mm. However, the best uniformity was found for the shortest target-to-substrate distance. Currently, the carriers are populated with SPO plates within an area of ~310 mm in the vertical direction times ~255 mm in the horizontal direction where the coating uniformity is measured to better than 5%. The mirror plate capacity of the BS1500S is between 168–336 per coating run depending on the mirror plate dimension (expecting 500 coating runs for flight production). For Athena the mirror dimensions vary as a function of the radial position in the telescope, the inner mirrors long and narrow and the outer mirrors wide and short, demanding the carrier design to be adjustable to minimize production cost.

2.2. Sample preparation

For cost reasons, we did not use SPO plates in this experiment. Instead we used double-side polished silicon rectangular substrates with a crystal orientation <100>, a thickness of 775±25 μm and dimensions 70 mm × 10 mm (L × W). These silicon substrates were considered sufficiently representative for the work described here. The samples were plasma cleaned with a power of 1000 W for 15 min in a mixed oxygen/nitrogen atmosphere prior to coating as further described in [25]. For these particular samples the plasma cleaning process ensured a surface roughness lower than 0.4 nm. We produced four single layer samples aiming for the four different thicknesses presented in Table 1.

The parameter settings used to produce the coated samples are given in Table 2. The power densities are based on the settings applied for the R&D of the thin films in the sputtering machine at DTU Space. The target dimensions is approximately three times the area of the targets used at DTU Space, resulting in an increase of the sputtered flux by a factor three. The dynamic deposition rates of the iridium and boron carbide films are derived from XRR measurements to ~6.0 nm × m/min and ~1.0 nm × m/min, respectively.

OSA®
The Optical Society

Table 1. Thin film coated samples.

Sample ID	Material	Aimed thickness (nm)
cs00002	Iridium	10.0
cs00004	Iridium	30.0
cs00006	Boron carbide	8.0
cs00008	Boron carbide	24.0

Table 2. Deposition parameters of sputtered iridium and boron carbide thin films.

Material	Working pressure (mbar)	Power (W)	Voltage (V)	Current (A)	Power density (W/cm^2)
Iridium	3.5×10^{-3}	1860	600	3.10	3.10
Boron carbide	3.5×10^{-3}	3200	705	4.54	5.17

2.3. Data acquisition

2.3.1. X-ray reflectometry

Precise reflectivity measurements in the XUV region were carried out using at–wavelength metrology facility with 11–axis Reflectometer end station coupled with Optics Beamline at BESSY-II synchrotron radiation source center [26]. All samples were measured ~14 months after thin film deposition with linear s–polarized light with a polarization purity better than 99.7% for the used energy range. We performed X-ray reflectometry at 2 fixed energies (1 keV and 1.487 keV) by varying the incidence angle and 1 fixed angle by varying the energy in a range from 50 –800 eV.
The beam cross section in focus on sample position was 0.36 mm × 0.25 mm (FWHM, W × H) and its divergence was 0.5 mrad × 3.6 mrad (W × H). These parameters are sufficient to avoid any significant increase of the beam size up to the detectors positioned 310 mm downstream. This enable us to receive specular reflection and most of the scattered part of reflected beam on the detector with active area of 4 mm × 4 mm. The same detector was used for measurements both reflected and incident beams. The spectral purity of the incident beam from high order diffractions of the monochromator grating was maintained better than 99.99% by an efficient high order suppression system installed in the beamline [27]. The accuracy of energy scale is in limits of ±0.02%, it is supported by calibration on more than 50 energy reference points distributed over whole working energy range of the beamline. Sample surface alignment in respect to the beam was carried out by 6-axis tripod system with position accuracies of 500 nm in translations and 1" in rotations. The tripod with sample stage is driven by a Huber 411 goniometer to change incident angle within -180° – +180° with position accuracy of 3.6" [28]. The accuracy of angle between incident beam and sample surface is also affected by sample surface flatness and the beam divergence. For this study we assumed that it is better than 0.02°. The beam intensity in–time stability is between 0.01% and 0.04% depending on heat load on first beamline focusing mirror.

2.3.2. X–ray photoelectric spectroscopy

The elemental properties of thin films are of great importance for the performance of X–ray optics. The thin films are composed of elements which exhibit absorption edges due to excitation of the atom in the Athena energy range. The same elements display photoelectric emission lines in X–ray photoelectron spectroscopy.

OSA® The Optical Society

We acquired XPS data using a Thermo Scientific K–Alpha system operating with a monochromized Al Kα beam (1486.6 eV) at a take–off angle of 90°. The data were collected nine months after thin film deposition and the samples were stored in ambient atmosphere. We used two different scanning modes (survey scans and high–resolution scans) and were analyzed using the CasaXPS software. The data were processed using a Shirley background and deconvoluted with appropriate line shapes (Gaussian–Lorentzian or an asymmetric Lorentzian).
The energy resolution of the survey scans is 1 eV. This mode was used to scan the energy range from 50–800 eV. For the high–resolution scans, we used an energy resolution of 0.1 eV within narrow energy bands for specific energies. To investigate the depth profile of the thin film, we performed iterative ion etching using argon to remove small amount of thin film layers. In the depth profile graphs, layer #1 indicates the surface of the thin film. For the scanning of non–conductive materials (boron carbide), we employed a combination of electrons and low–energy argon ions to neutralize charge build–up on the film surface arising from the bombardment of X–rays.

3. Results and Discussion

3.1. The chemical composition of single layer iridium and boron carbide films

By investigating the energy range from 50–800 eV, using the two different techniques, we illustrate the correlation between the absorption edges and the emission lines of the elements composing the thin films. The Ar 2p and Ar 2s emission lines (Fig. 2) observed in the iridium and boron carbide films at binding energies 242.1 eV and 319.1 eV, originate from the XPS depth profiling technique where argon is bombarded into the thin film to remove layers of the thin films resulting in the presence of argon [29]. The fact that the argon is not present in the film surface nor the XRR spectra confirm this explanation.

The iridium film exhibits absorption edges at 61 eV and 64 eV originating from the outermost atomic orbital of the iridium (Fig. 2 left). The emission lines of the peak doublet that arise from the spin properties of the electrons are observed at the exact same energies as the absorption lines in the XRR data. An interesting observation is that the absorption lines of Ir 5s, 4d, 4p and 4s are not visible in the reflectivity curve. We assume that the absorption intensity is washed out in the signal.
Absorption edges from carbon and oxygen are observed at 284.4 eV and 531.5 eV, respectively. Carbon and oxygen are only present on the surface of the iridium film. These originate from the ambient atmosphere and are usually referred to as a mix of hydrocarbons [30] and water (Fig. 3 III and V). The observation of hydrocarbons on the iridium surface supports the 3–layer model described in the XRR modeling.
The iridium film shows no signs of other elements in the film interior as shown in Fig. 3 I. In Fig. 3 II, the silicon emission lines are visible after three etching iterations and in Layer #4, the native silicon oxide on the substrate surface is detected by the shift in peak position towards a higher energy.

For the single layer boron carbide film we observe absorption edges of boron, carbon, nitrogen, oxygen and iron in the reflectivity curve measured at a grazing incidence of 1.4 degrees (Fig. 2 right). The absorption lines observed in the figure are in agreement with the emission lines observed in the XPS spectra. We observe that the boron carbide film surface is contaminated with oxygen and nitrogen when exposed to the ambient atmosphere. We observe a chemical reaction between the boron, carbon, nitrogen and oxygen elements in the boron carbide film surface. If this reaction is instant when exposed to the ambient atmosphere or if it occurs with time has not been studied yet. As mentioned previously, the samples were measured nine months after thin film deposition. Within this time-frame we observe an evolution in the surface of the

OSA®
The Optical Society

boron carbide film. This is supported by the high–resolution XPS spectra presented in Fig. 3 (VII–XII). A deconvolution of the boron spectra indicate the main chemical state at 188.1 eV which we assign to boron carbide (B–C) and the shoulder at 189.8 eV assigned to boron sub-oxide (B–C–O). Similar results have been shown in [31, 32], where the B4C component was reported at ~188.4 eV and ~188.6 eV, respectively. The boron sub-oxide state is a result of a chemical surface reaction that can originate from the atmosphere inside the sputtering machine during deposition, when the film is exposed to the ambient atmosphere or a combination of the two.
The carbon spectra exhibit a strong chemical reaction between carbon, boron, nitrogen and oxygen (Fig. 3 IX). We assign the multiple chemical states observed in Layer #1 at 282.5 eV, 284.4 eV, 288.0 eV, 292.7 eV and 295.5 eV to B–C, C–H for the lower energies while the three higher energies are appointed to carbon oxides (C–O) states [8, 33, 34]. We observe nitrogen emission lines in the surface of the boron carbide film located at 400 eV which is likely a combination of C–N and N–H chemical bonds [35]. Unlike in the iridium film, we observe Fe 2s/Fe 2p peaks in the boron carbide film at 707 eV and 720 eV which originates from the iron contamination in the target material. The oxygen emission lines are visible throughout the whole film with a lower amount of oxygen in the interior and the highest amount in the surface of the film. Under the assumption that the boron carbide film has voids, the interior part of the film may be exposed to oxygen in the ambient atmosphere. Another likely explanation is that the oxygen from the ambient atmosphere diffuses into the film with time.

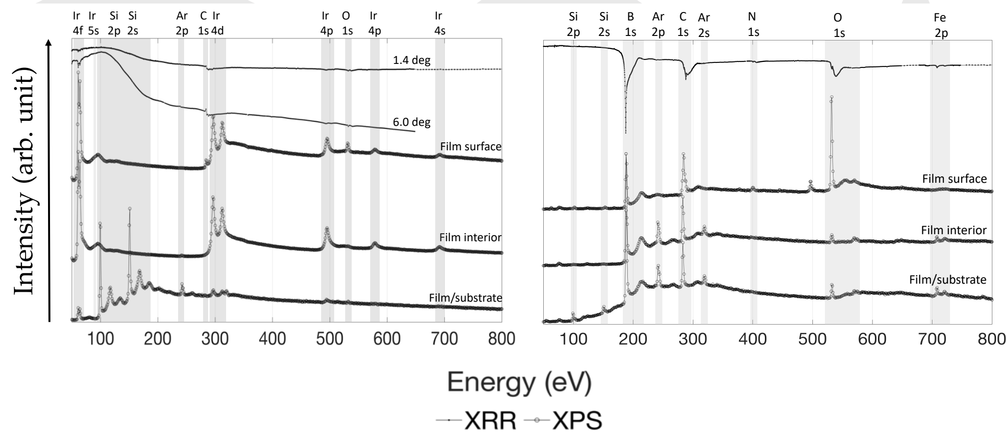

Fig. 2. XRR data shown with XPS data to indicate the chemical composition of the single layer iridium sample **cs00002** (left) and the single layer boron carbide sample **cs00008** (right).

The Optical Society ®

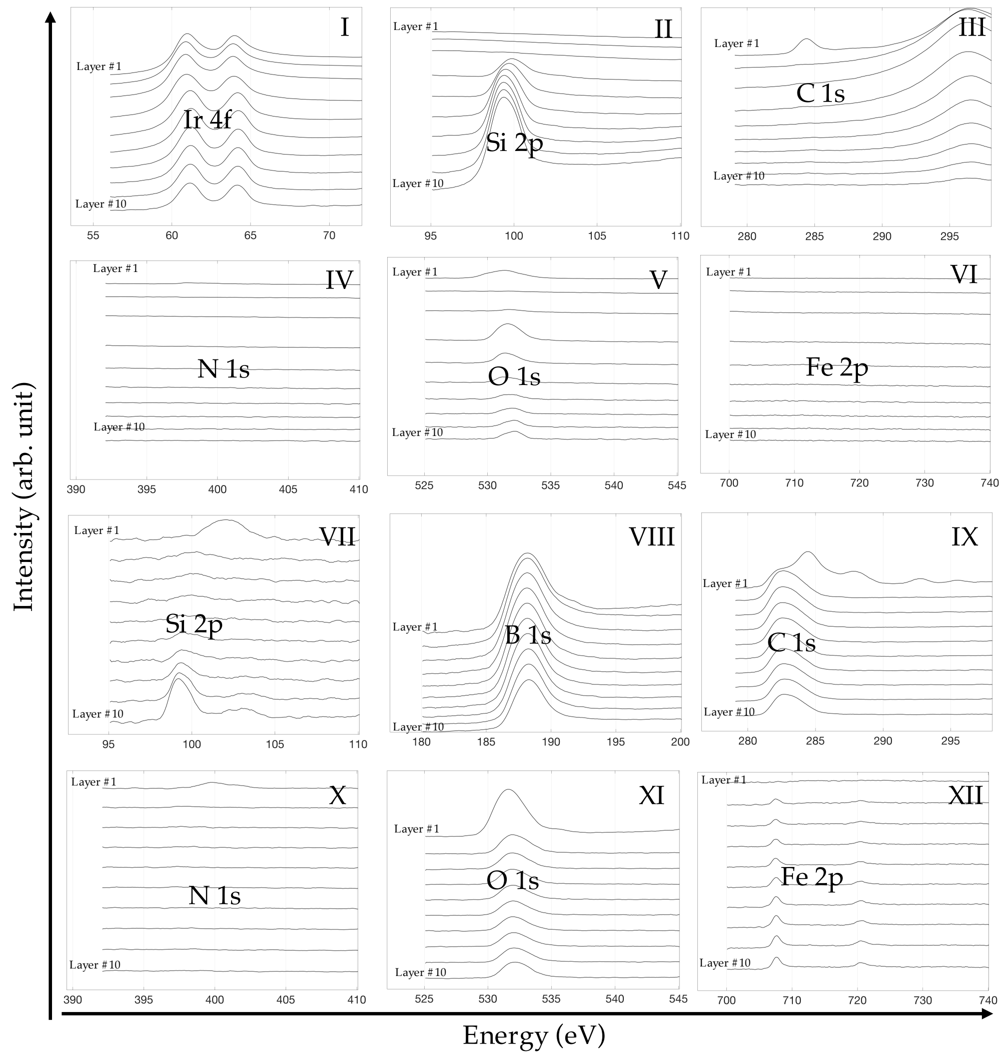

Fig. 3. High–resolution XPS measurements of the single layer iridium sample, **cs00002** (I–VI) and the single layer boron carbide film, **cs0008** (VII–XII), using the depth profiling technique.

3.2. Modeling of X–ray reflectivity data acquired at 1000 eV and 1487 eV

We used the IMD software [36], based on the Fresnel equations, to analyze the XRR data and derive the thin film properties. For obtaining the best–fit parameters, we used the differential evolution algorithm [37] included in the software. The model structures are based on the XPS analyses presented in Section 3.1 which indicate a more complex film structure than a single layer. We considered two different models to obtain the best–fit of the iridium data and the boron carbide data.

The iridium films were modeled using a 2–layer model (model A and B, with the only difference between the two models being the density) composed of $Si/SiO_2/Ir$ and a 3–layer model (model C) composed of $Si/SiO_2/Ir/C–H–O$. The boron carbide films were modeled using a similar approach where the 2–layer model (model D) is composed of $Si/SiO_2/B_4C$ and the 3–layer model (model E) is composed of $Si/SiO_2/B_4C/B–C–O$. In all models, we fixed the SiO_2 thickness to 2.0 nm which is common for native oxide grown on the silicon surface [38]. We coupled the Si and SiO_2 roughnesses, due to the complexity of the models and the correlation between fit parameters.

We approached the modeling by allowing the density, thickness and roughness parameters to vary for each model considered. Table 3 shows the best–fit parameters of the single layer iridium films. We observed a discrepancy between the model and the data that is large near the critical angle when allowing the density to vary in model A. The best–fit density converged to low values between 21.2 g/cm^3 and 22.2 g/cm^3 (bulk density of hot pressed iridium is 22.56 g/cm^3 [39]). We consider the 2–layer model insufficient to describe the data due to this large variation.

For model C, we assumed an overlayer of C–H–O compound(s). The research performed in [40] shows that several compounds of C–H–O chemical states are likely to originate from atmospheric contaminants adsorbed to the surface of the iridium film. Most of these chemical compounds consisting of C–H–O are listed with a density between 0.9–1.0 g/cm^3. Based on this, we fixed the density of the overlayer to 1.0 g/cm^3 which is in agreement with the overlayer density presented in [41].

Using model C to describe the data, we obtained an iridium density of 22.4 g/cm^3 which is close to 99% of bulk density whereas [42] measured the density of a 30 nm magnetron sputtered iridium film to greater than 95% of bulk density. The fitted overlayer thickness is between 1.0–1.7 nm for the two different iridium thicknesses. We observe that the overlayer thickness derived from the 1000 eV XRR data is slightly higher than the overlayer thickness derived from the 1487 eV XRR data by ~0.4 nm for both iridium thicknesses.

We fixed the best–fit density to 22.4 g/cm^3 in model B which was obtained from model C, and allowed the thickness and the roughnesses to vary, to validate that the 3–layer model describes the data better than the 2–layer model. Observed in Fig. 4 (I–IV), model B shows an improvement near the critical angle. However, model C shows significantly lower residuals in both energy scans for both film thicknesses. In the valleys and tops of the Kiessig fringes, we observe the largest discrepancy between the model and the data which may be due to a substrate waviness or a small film non–uniformity along the measurement direction.

OSA ®
The Optical Society

Table 3. Best–fit parameters derived from applying models A, B and C to the data acquired for the single layer iridium films (**cs00002** and **cs00004**). The parameters allowed to vary are presented in bold. [a,b] are coupled parameters. [c] fixed values based on a priori assumptions (described in text). [d] denotes the density of native silicon oxide. [e] denotes the density based on the best–fit parameter derived from model C.

Sample ID	Energy (eV)	Model	Layer	Composition	Thickness (nm)	Density (g/cm^3)	Roughness (nm)
cs00002	1000	A	Top	Ir	**10.0**	**22.2**	**0.36**
			Intermediate 1	SiO_2	2.0[c]	2.65[d]	**0.39**[a]
			Substrate	Si	-	-	**0.39**[a]
		B	Top	Ir	**10.0**	22.4[e]	**0.35**
			Intermediate 1	SiO_2	2.00[c]	2.65[d]	**0.32**[a]
			Substrate	Si	-	-	**0.32**[a]
		C	Top	C-H-O	**1.4**	1.0[c]	**0.30**[b]
			Intermediate 2	Ir	**10.0**	**22.4**	**0.30**[b]
			Intermediate 1	SiO_2	2.0[c]	2.65[d]	**0.39**[a]
			Substrate	Si	-	-	**0.39**[a]
cs00002	1487	A	Top	Ir	**10.0**	**21.8**	**0.26**
			Intermediate 1	SiO_2	2.0[c]	2.65[d]	**0.39**[a]
			Substrate	Si	-	-	**0.39**[a]
		B	Top	Ir	**10.0**	22.4[e]	**0.26**
			Intermediate 1	SiO_2	2.0[c]	2.65[d]	**0.39**[a]
			Substrate	Si	-	-	**0.39**[a]
		C	Top	C-H-O	**1.0**	1.0[c]	**0.23**[b]
			Intermediate 2	Ir	**10.0**	**22.4**	**0.23**[b]
			Intermediate 1	SiO_2	2.0[c]	2.65[d]	**0.39**[a]
			Substrate	Si	-	-	**0.39**[a]
cs00004	1000	A	Top	Ir	**30.8**	**21.6**	**0.39**
			Intermediate 1	SiO_2	2.0[c]	2.65[d]	**0.36**[a]
			Substrate	Si	-	-	**0.36**[a]
		B	Top	Ir	**30.8**	22.4[e]	**0.40**
			Intermediate 1	SiO_2	2.0[c]	2.65[d]	**0.35**[a]
			Substrate	Si	-	-	**0.35**[a]
		C	Top	C-H-O	**1.7**	1.0[c]	**0.36**[b]
			Intermediate 2	Ir	**30.8**	**22.4**	**0.36**[b]
			Intermediate 1	SiO_2	2.0[c]	2.65[d]	**0.36**[a]
			Substrate	Si	-	-	**0.36**[a]
cs00004	1487	A	Top	Ir	**30.8**	**21.3**	**0.31**
			Intermediate 1	SiO_2	2.0[c]	2.65[d]	**0.40**[a]
			Substrate	Si	-	-	**0.40**[a]
		B	Top	Ir	**30.8**	22.4[e]	**0.31**
			Intermediate 1	SiO_2	2.0[c]	2.65[d]	**0.40**[a]
			Substrate	Si	-	-	**0.40**[a]
		C	Top	C-H-O	**1.4**	1.0[c]	**0.29**[b]
			Intermediate 2	Ir	**30.8**	**22.4**	**0.29**[b]
			Intermediate 1	SiO_2	2.0[c]	2.65[d]	**0.36**[a]
			Substrate	Si	-	-	**0.36**[a]

OSA® The Optical Society

We applied a similar approach to model the boron carbide data. However, the chemical composition of the boron carbide films is more complex than the iridium films because the top surface of the boron carbide film chemically reacts with the ambient atmosphere at room temperature [43]. The best–fit parameters derived from model D, given in Table 4, indicate a film density of ~2.3 g/cm^3 which is about 10% lower than the bulk density. Similar to the iridium 2–layer modeling, we demonstrate that the 2–layer model is insufficient to describe the data and that the density and thickness values are averages of the entire films.

Fig. 4 (V–VIII), indicate that model E is an improvement compared to model D. However, the residuals are large in both cases. The top–layer derived from model E has a thickness of ~2.5 nm and a density of ~1.7 g/cm^3. The intermediate layer 2 has a density of ~2.6 g/cm^3 which is a few percent higher than the nominal density, which could be explained by the iron contamination in the film, or a limitation of the model. We assume that the boron carbide coating has a gradient density throughout the film which is likely due to the film growth mechanism of the boron and carbon elements.

Table 4. Best–fit parameters derived from applying models D and E to the data acquired for the single layer boron carbide films (**cs00006** and **cs00008**). The parameters allowed to vary are presented in bold. [a] denotes the coupled roughness parameters which are set to 0.35 nm. [b] fixed values based on a priori assumptions (described in text). [c] denotes the density of native silicon oxide.

Sample ID	Energy (eV)	Model	Layer	Composition	Thickness (nm)	Density (g/cm^3)	Roughness (nm)
		D	Top	B-C	**6.0**	**2.2**	**0.45**
			Intermediate 1	SiO_2	2.0[b]	2.65[c]	0.35[a]
			Substrate	Si	-	-	0.35[a]
cs00006	1000	E	Top	B-C-O	**2.2**	**1.6**	**0.32**
			Intermediate 2	B-C	**3.6**	**2.5**	**0.92**
			Intermediate 1	SiO_2	2.0[b]	2.65[c]	0.35[a]
			Substrate	Si	-	-	0.35[a]
		D	Top	B-C	**5.5**	**2.3**	**0.47**
			Intermediate 1	SiO_2	2.0[b]	2.65[c]	0.35[a]
			Substrate	Si	-	-	0.35[a]
cs00006	1487	E	Top	B-C-O	**1.8**	**1.6**	**0.17**
			Intermediate 2	B-C	**3.8**	**2.6**	**1.40**
			Intermediate 1	SiO_2	2.0[b]	2.65[c]	0.35[a]
			Substrate	Si	-	-	0.35[a]
		D	Top	B-C	**19.5**	**2.3**	**0.43**
			Intermediate 1	SiO_2	2.0[b]	2.65	0.35[a]
			Substrate	Si	-	-	0.35[a]
cs00008	1000	E	Top	B-C-O	**2.8**	**1.7**	**0.30**
			Intermediate 2	B-C	**16.7**	**2.6**	**1.11**
			Intermediate 1	SiO_2	2.0[b]	2.65[c]	0.35[a]
			Substrate	Si	-	-	0.35[a]
		D	Top	B-C	**19.3**	**2.4**	**0.42**
			Intermediate 1	SiO_2	2.0[b]	2.65	0.35[a]
			Substrate	Si	-	-	0.35[a]
cs00008	1487	E	Top	B-C-O	**3.2**	**1.8**	**0.19**
			Intermediate 2	B-C	**16.0**	**2.6**	**1.56**
			Intermediate 1	SiO_2	2.0[b]	2.65[c]	0.35[a]
			Substrate	Si	-	-	0.35[a]

OSA ® The Optical Society

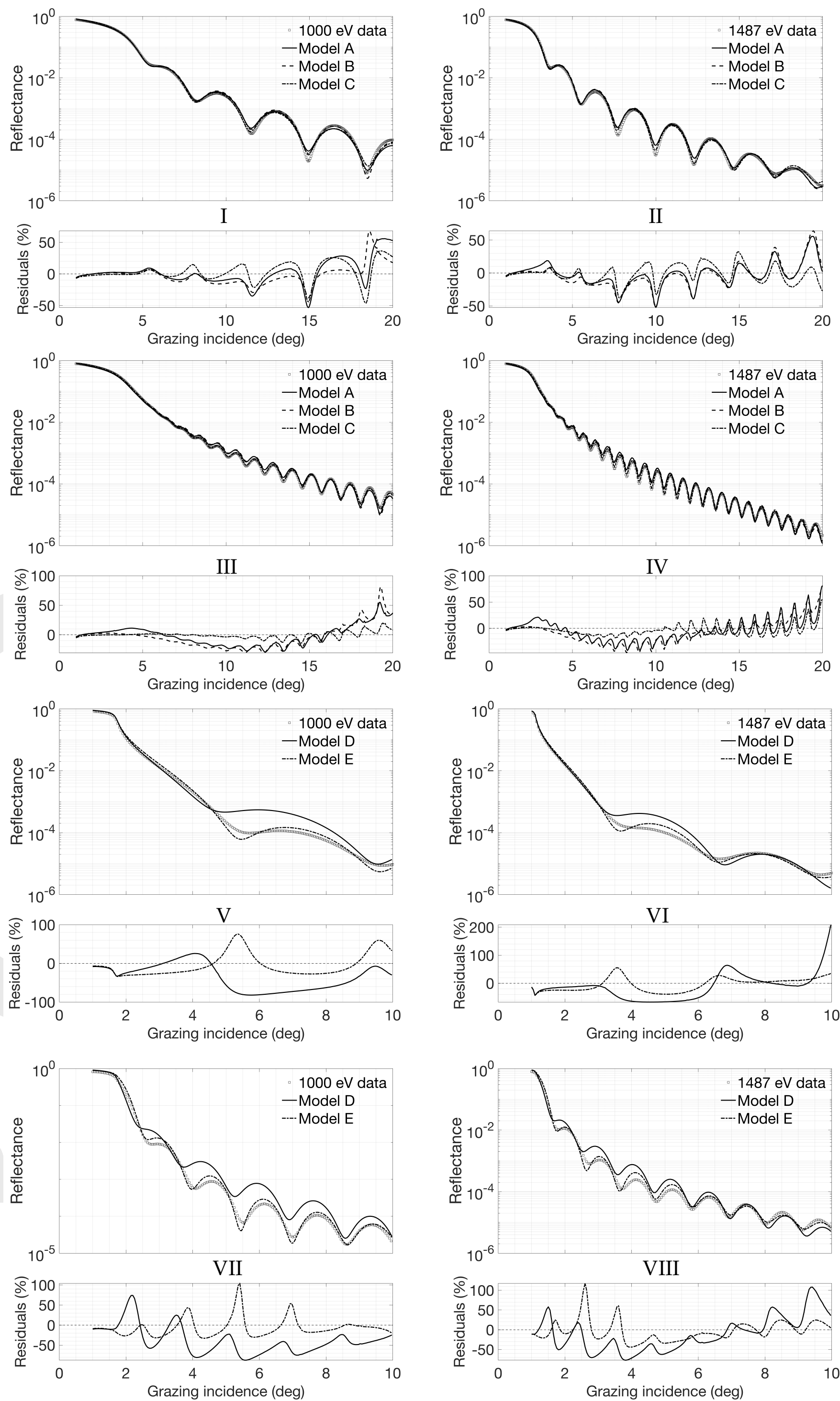

Fig. 4. XRR data acquired at two different energies, 1000 eV and 1487 eV, and the best-fit models. I and II are XRR performed on the single layer iridium sample (**cs00002**), III and IV are XRR performed on the single layer iridium sample (**cs00004**), V and VI are XRR performed on the single layer boron carbide sample (**cs00006**), and VII and VIII are XRR performed on the single layer boron carbide sample (**cs00008**).

4. Conclusion

We fabricated and analyzed single layer iridium and boron carbide thin films with focus on the chemical composition, density, thickness and roughness of the materials. We investigated the materials independently due to limitations of modeling the low-Z material using XRR when it is configured in a bilayer configuration. The limitation is that the signal from the iridium is dominant in the reflectivity spectrum which makes the features of the low-Z material less prominent in the modeling, even at lower energy XRR scans. Another reason is that some mirrors in the Athena optics may only be coated with a single layer of iridium and it is therefore important to understand the composition of iridium alone and the influence of hydrocarbons on the reflective surface.
We tested 2–and 3–layer models to describe the XRR data and concluded that the 3–layer model fit the boron carbide and iridium data best. The 3–layer model composed of Si/SiO_2/Ir/C–H–O describes the single layer iridium best when assuming a few nanometer thick overlayer with a density of 1.0 g/cm^3 originating from atmospheric contaminants that adsorbed to the surface of the iridium film. The best–fit density for both iridium film thicknesses was 22.4 g/cm^3, which corresponds to ~99% of the nominal density. The best–fit boron carbide density when applying the 3–layer model composed of Si/SiO_2/B_4C/B–C–O was ~0.1 g/cm^3 higher than nominal, which we explained by the iron contamination and the limitations of the modeling. The top–layer of the boron carbide films oxidized when exposed to the ambient atmosphere which was suggested by the XRR modeling and confirmed by the XPS analyses. We observed oxygen emission lines throughout the whole film, which may be diffusion of oxygen into the boron carbide film or a signal from the native SiO_2 on the surface of the silicon substrate. We also showed the correlation between the absorption edges in the XRR spectrum and the emission lines in the XPS spectrum. The absorption edges and the emission lines are in agreement for both the iridium and boron carbide films. The oxygen and carbon contamination has a clear effect on the reflectance curve of the single layer iridium films. The oxidation of the boron carbide surface is revealed by the emission line spectrum and the absorption edge in the reflectance is prominent.
For further investigations of the thin film materials for the X-ray optics application we conclude that the characterization methods presented are key in obtaining detailed information of the properties of the thin films.

5. Acknowledgement

This work was funded by the European Space Agency under contract: 4000116080/15/NL/BW.

6. Disclosures

The authors declare no conflicts of interest.

References

1. K. P. Singh, "Grazing incidence optics for X-ray astronomy: X-ray optics," J. Opt. (india) **40**, 88–95 (2011).
2. M. Bavdaz *et al.*, "Development of the ATHENA Mirror," Proc. SPIE (2018).
3. K. Nandra *et al.*, "The Hot and Energetic Universe: A White Paper presenting the science theme motivating the Athena+ mission," (2013).
4. N. J. Westergaard *et al.*, "On X-ray telescopes in general and the Athena optics in particular," Nucl. Instruments Methods Phys. Res. Sect. A: Accel. Spectrometers, Detect. Assoc. Equip. **873**, 5–11 (2017).
5. G. Pareschi *et al.*, "Astronomical soft X-ray mirrors reflectivity enhancement by multilayer coatings with carbon overcoating," Proc. SPIE **5488**, 481–491 (2004).
6. J. I. Larruquert *et al.*, "Optical properties of hot-pressed B4C in the extreme ultraviolet," Appl. Opt. **39**, 1537–1540 (2000).
7. D. D. M. Ferreira *et al.*, "Performance and stability of mirror coatings for the ATHENA mission," Proc. SPIE **10699**, 106993K (2018).
8. T. Hu *et al.*, "Structures and properties of disordered boron carbide coatings generated by magnetron sputtering," Thin Solid Films **332**, 80–86 (1998).

OSA® The Optical Society

9. N. Kaiser, “Review of the fundamentals of thin-film growth,” Appl. Opt. **41**, 3053–60, 3053–3060 (2002).
10. J. A. Thornton, “The microstructure of sputter-deposited coatings,” J. Vac. Sci. Technol. a (vacuum, Surfaces, Films) **4**, 3059–65, 3059–3065 (1986).
11. M. Collon *et al.*, “Silicon pore optics mirror module production and testing,” Proc. SPIE **10699**, 106990Y (2018).
12. S. Svendsen, “Development and characterization of X-ray mirror coatings for the ATHENA observatory,” Ph.D. thesis, Technical University of Denmark (2020). Unpublished.
13. R. A. M. Keski-Kuha *et al.*, “Effects of space exposure on ion-beam-deposited silicon-carbide and boron-carbide coatings,” Appl. Opt. **37**, 8038–8042 (1998).
14. S. Massahi, “Industrialization of the mirror plate coatings for the ATHENA mission,” Ph.D. thesis, Technical University of Denmark (2019).
15. S. Swann, “Magnetron sputtering,” Phys. Technol. **19**, 67–75 (1988).
16. P. Martin, *Handbook of Deposition Technologies for Films and Coatings* (Elsevier Inc., 2010).
17. F. E. Christensen *et al.*, “Coatings for the NuSTAR mission,” Proc. SPIE **8147**, 81470U (2011).
18. A. C. Jakobsen *et al.*, “Preliminary coating design and coating developments for ATHENA,” Proc. SPIE **8147**, 81470T (2011).
19. D. D. M. Ferreira *et al.*, “Development and characterization of coatings on Silicon Pore Optics substrates for the ATHENA mission,” Proc. SPIE **8443**, 84435E (2012).
20. D. D. M. Ferreira *et al.*, “Coating optimization for the ATHENA+ mission,” Proc. SPIE **8861**, 886112 (2013).
21. D. D. M. Ferreira *et al.*, “X-ray mirror development and testing for the ATHENA mission,” Proc. SPIE **9905**, 99055K (2016).
22. S. Massahi *et al.*, “Development and production of a multilayer-coated X-ray reflecting stack for the Athena mission,” Proc. Space Telesc. Instrumentation 2016: Ultrav. To Gamma Ray **9905**, 99055P (2016).
23. D. D. M. Ferreira *et al.*, “Design, development, and performance of x-ray mirror coatings for the Athena mission,” Proc. SPIE (2017).
24. A. Vickery *et al.*, “Collimated Magnetron Sputter Deposition for Mirror Coatings,” X-ray Opt. Instrumentation **2008**, 792540 (9 pp.), 792540 (9 pp.) (2008).
25. S. Massahi *et al.*, “Investigation of Photolithography Process on SPOs for the ATHENA Mission,” Proc. Spie, Int. Soc. for Opt. Eng. **9603**, 96030M (2015).
26. A. Sokolov *et al.*, “At-wavelength metrology facility for soft X-ray reflection optics,” Rev. Sci. Instruments **87**, 052005 (2016).
27. A. Sokolov *et al.*, “Efficient high-order suppression system for a metrology beamline,” J. Synchrotron Radiat. **25**, 100–107 (2018).
28. F. SchÃďfers *et al.*, “The at-wavelength metrology facility for UV-and XUV-reflection and diffraction optics at BESSY-II,” J. Synchrotron Radiat. **23**, 67–77 (2016).
29. “Thermo Scientific XPS: Argon,” https://www.jp.xpssimplified.com/elements/argon.php.
30. L. Calvo-Barrio *et al.*, “Photoelectron spectroscopy for surface analysis: X-ray and UV excitation,” (2012).
31. H. Jiang *et al.*, “The influence of residual gas on boron carbide thin films prepared by magnetron sputtering,” Appl. Surf. Sci. **257**, 9946–9952 (2011).
32. R. Soufli *et al.*, “Optical constants of magnetron-sputtered boron carbide thin films from photoabsorption data in the range 30 to 770 eV,” Appl. Opt. **47**, 4633–4639 (2008).
33. Q. Yang *et al.*, “Effect of nitrogen pressure on structure and optical properties of pulsed laser deposited BCN thin films,” Surf. Coatings Technol. **204**, 1863–1867 (2010).
34. E. Ech-Chamikh *et al.*, “XPS study of amorphous carbon nitride (a-C : N) thin films deposited by reactive RF sputtering,” Sol. Energy Mater. Sol. Cells **90**, 1420–1423 (2006).
35. P. Y. Tessier *et al.*, “Carbon nitride thin films deposited by reactive plasma beam sputtering,” Surf. Coatings Technol. **125**, 295–300 (2000).
36. D. L. Windt, “IMD - Software for modeling the optical properties of multilayer films,” COMPUTERS IN PHYSICS **12**, 360–370 (1998).
37. M. BjÃűrck, “Fitting with differential evolution: An introduction and evaluation,” J. Appl. Crystallogr. **44**, 1198–1204 (2011).
38. M. Morita *et al.*, “Growth of native oxide on a silicon surface,” J. Appl. Phys. **68**, 1272–1281 (1990).
39. J. Arblaster, “Densities of osmium and iridium. recalculations based upon a review of the latest crystallographic data,” Platinum Met. Rev. **33**, 14–16 (1989).
40. J. P. Sheehy *et al.*, *Handbook of Air Pollution*, Environmental health series: Air pollution (U.S. Department of Health, Education, and Welfare, Public Health Service, Bureau of Disease Prevention and Environmental Control, National Center for Air Pollution Control, 1968).
41. D. E. Graessle *et al.*, “Optical constants from synchrotron reflectance measurements of AXAF witness mirrors 2 to 12 keV,” in *Grazing Incidence and Multilayer X-Ray Optical Systems,* vol. 3113 R. B. Hoover and A. B. C. W. II, eds., International Society for Optics and Photonics (SPIE, 1997), pp. 52 – 64.
42. S. Romaine *et al.*, “Measurements of the hard-x-ray reflectivity of iridium,” Appl. Opt. **46**, 185–189 (2007).
43. P. N. Rao *et al.*, “Investigation of composition of boron carbide thin films by resonant soft x-ray reflectivity,” Surf. Coatings Technol. **334**, 536–542 (2018).

OSA ® The Optical Society